

Results from the GMT Ground-Layer Experiment at the Magellan Telescopes

A. Athey^a, S. Shectman^a, M. Phillips^b, J. Thomas-Osip^b

^aCarnegie Observatories, Pasadena, CA 91101-1209, USA;

^bLas Campanas Observatory, Carnegie Observatories, Casilla 601, La Serena, Chile;

ABSTRACT

We present results from our two year study of ground-layer turbulence as seen through the 6.5-meter Magellan Telescopes at Las Campanas Observatory. The experiment consists of multiple, moderate resolution, Shack-Hartmann wavefront sensors deployed over a large 16 arcminute field. Over the two years of the experiment, the ground-layer turbulence has been sampled on eleven nights in a variety of seeing and wind conditions. On most nights the ground-layer turbulence contributes 10% to the total visible-band seeing, although a few nights exhibit ground-layer contributions up to 30%. We present the ground-layer turbulence on the sampled nights as well as a demonstration of its strength as a function of field size. This information is combined with data from a MASS-DIMM seeing monitor adjacent to the Magellan Telescopes to infer the annual ground-layer contribution to seeing at Las Campanas.

Keywords: Adaptive Optics, Ground-Layer, GLAO, Seeing

1. INTRODUCTION

The concept of ground-layer adaptive optics correction (GLAO) is to make a modest improvement in image quality over a large field of view (many arcmin) by compensating for the turbulence in the lowest layers of the atmosphere. GLAO is complementary to full-atmosphere adaptive optics correction (AO), which delivers diffraction-limited imaging, but only over small fields of view (< 1 arcmin).

Recent studies of the atmosphere at astronomical sites have been conducted using a variety seeing monitors, and also with balloons carrying micro-thermal sensors.¹⁻⁶ A number these studies provide measurements of both the total seeing and the distribution of turbulence as a function of altitude. The new results suggest that typically more than half of the turbulent power in the atmosphere occurs at low altitude ($\lesssim 1.0$ km). This ground-layer is thought to arise from the interaction of moving air with local topography, which may differ from site to site depending on wind direction and ground contour upstream of the telescope.

The presence of a strong, low altitude turbulence layer provides an opportunity to improve the seeing using an AO system with modest operating parameters.⁷ Near the ground, the wind speed is low so the crossing time for a turbulent cell is typically on the order of ten milliseconds or more. Because the effective height of the ground layer is largest for the largest turbulent scales, a GLAO system favors correction of the lowest order modes. For atmospheric layers near the telescope, the isoplanatic angle will be large. Thus, a GLAO system might operate at low frequency (100 Hz) and low order (< 50 modes on a 6.5-m telescope) while significantly improving the image quality over a large field of view (many arcmin). Initial GLAO models predicted a gain of a factor of two in image size over fields of 10 arcmin or more, resulting in a factor of four gain in sensitivity for background limited observations.^{7,8} The potential of GLAO correction is evident, however most of the work to date has consisted of modeling based on a few atmospheric measurements. Only limited amounts of data have been taken at the telescope.

Although several on-going studies reveal at least some information about ground-layer turbulence,^{9,10} none of the current experiments provides adequate empirical measurements of the parameters and performance of a GLAO system. Early laser-tomography experiments, for example, are restricted to smaller fields of view. Since in any event different observatory sites might be expected to exhibit different ground-layer conditions, we have chosen to conduct an experiment to directly measure the effect of ground-layer turbulence at the Magellan Telescopes. This experiment was conducted as part the Giant Magellan Telescope (GMT) project, in order to study the implications of GLAO for the design of GMT and its instrumentation.

2. GLAO INSTRUMENT/EXPERIMENT DESCRIPTION

We have developed a system of multiple Shack-Hartmann wavefront sensors to investigate the ground-layer of the atmosphere as seen through one of the 6.5 meter Magellan telescopes. Up to four separate wavefront sensors are attached to a machined plate in the telescope focal plane at the locations of stars in a few bright asterisms (both real clusters and random groupings) selected at convenient locations around the sky. The cameras operate at a frame rate of 100 Hz. The separations between stars range from a minimum of 4.5 arcminutes, set by mechanical interference between adjacent units, to 16 arcminutes, set by the field of view of the standard Magellan guider package and the size of the machined plate. The system uses off-the-shelf components to minimize cost and development time at the expense of sensitivity.

The optics consist of a stock achromatic field lens and a lenslet array which produces multiple images of the star directly on the detector. The A.O.A. Inc. lenslet array has a pitch of $203\mu\text{m}$ and a focal length of 5.8 mm. The optics sample the pupil in an 11x11 square grid, resulting 90 usable subapertures which are inside the perimeter of the primary mirror and unobscured by the shadow of the secondary. The subapertures are 59 cm square at the primary mirror, which is somewhat larger than the coherence scale so there is some seeing within a subaperture. The original choice of subaperture size was motivated by the idea that it might be possible to implement a functional low-order, wide-field GLAO system based on natural guide stars.

The simplest algorithm for isolating the wavefront error contributed by the ground layer is just to average the outputs of multiple wavefront sensors distributed around the field of view. The analysis is simplified if the individual subapertures are accurately registered to identical pupil positions in all of the wavefront sensors. This requires both rotational alignment of the lenslet arrays and cameras, as well as x-y alignment of the lenslet arrays on the pupil. In order to accomplish the x-y alignment, the lenslet array is deliberately offset from the exact focus of the field lens. Each wavefront sensor is mounted on an x-y stage. Adjustment of the x-y position of the stage changes the positions of star images on the camera, but because the lenslet array is not quite at the focus of the field lens, the adjustment also changes the registration of the lenslet array on the pupil. In our wavefront sensors, a 1.0 arcsecond motion of the star corresponds to a $75\mu\text{m}$ motion on the detector. The spacing between subapertures is 2.6 arcseconds. However the motion required to change the alignment of the subapertures on the pupil is much larger: a displacement of 5 arcseconds will move the subaperture position about one-half of the distance between subapertures. Strictly speaking, the subaperture alignment should be referenced to the conjugate height of ground layer. This was accomplished by mounting a special pupil mask near the center of the Magellan secondary mirror. Since the telescope is Gregorian the conjugate image of the secondary is located about 60 m above the primary. The wavefront sensor mounts include an additional motion along the z-axis which is used to adjust the focus of the wavefront sensor (or equivalently the pitch of the Shack-Hartmann array on the detector) in order to compensate for the curvature of the telescope focal plane.

The cameras are commercial units purchased from Basler Vision Technologies. The Basler A602f cameras use a Micron CMOS detector (MT9V403C125STM) which has a fast readout (up to 200 full frames per second), but is relatively noisy (80 electron rms/pixel). The cameras have a trigger signal for camera synchronization and a firewire (IEEE 1394a) bus for data I/O, with 8 bits of output selectable within a 12-bit dynamic range. The CMOS detector has 9.9 micron pixels in a 656 by 491 format. In operation we read out a 312 by 312 section of the chip. With this region of interest, the maximum frame rate is 210 Hz, but in practice we operate between 100 and 128 Hz. After readout, the data are binned 2x2 which results in sub-apertures separated by 10 pixels, allowing for accurate centroiding and spot size measurements, and eliminating sub-aperture boundary crossings. Because of the high read noise, the wavefront sensors have an effective magnitude limit of 7.25 on the 6.5 meter Clay (Magellan 2) telescope. At maximum gain, variations in bias level within a frame are significant, but subtraction of a bias frame leaves the data flat to a few percent. The peak efficiency of the detector is 32% at 550 nm, and the system has an effective wavelength of 620 nm.

The Basler A602f camera follows an industry standard for firewire cameras (version 1.30 of the "1394 - based Digital Camera Specification" (DCAM) issued by the 1394 Trade Association). This allowed us to write our own control software on a linux-based PC using the open-source implementation of the DCAM specifications (libdc1394).

Each of the 4 cameras is attached to a separate computer, with a fifth computer to provide overall synchronization. The raw data rate is substantial at 0.5 Gigabyte/min/camera, but a few minutes of data are adequate

| Run | Date | JD | # Cameras | Separations (arcminutes) | Clay (arcsec) | DIMM (arcsec) | MASS (arcsec) | Wind Speed (mph) | Temp (C) |
|-----|----------|-------------|-----------|--------------------------------------|------------------|------------------|------------------|---------------------|-------------|
| 1 | 06/04/04 | 2453161.821 | 2 | 7.04 | 0.43 | N/A | N/A | 13 | 11.8 |
| 2 | 09/23/04 | 2453271.526 | 2 | 13.85 | 0.96 | N/A | N/A | 17 | 13.3 |
| 3 | 09/24/04 | 2453272.552 | 2 | 13.85 | 0.69 | 0.70 | 0.70 | 13 | 16.4 |
| 4 | 09/26/04 | 2453273.501 | 2 | 13.85 | 0.68 | 0.70 | 0.47 | 12 | 14.6 |
| 5 | 09/27/04 | 2453275.517 | 2 | 13.85 | 0.76 | 0.77 | 0.51 | 5 | 12.8 |
| 6 | 09/27/04 | 2453275.740 | 2 | 14.88 | 0.82 | 0.79 | 0.52 | 3 | 14.1 |
| 7 | 09/27/04 | 2453275.799 | 2 | 15.54 | 1.09 | 0.97 | 1.21 | 14 | 13.9 |
| 8 | 09/28/04 | 2453276.724 | 2 | 14.88 | 1.04 | N/A | N/A | 15 | 14.3 |
| 9 | 09/28/04 | 2453276.795 | 2 | 15.54 | 0.81 | 0.88 | 0.95 | 12 | 14.4 |
| 10 | 09/28/04 | 2453276.845 | 2 | 12.90 | 1.02 | 1.10 | 1.05 | 8 | 14.2 |
| 11 | 05/30/05 | 2453520.830 | 4 | 4.30, 7.35, 9.19, 9.41, 11.26, 15.60 | 0.69 | N/A | N/A | 7 | 15.7 |
| 12 | 05/31/05 | 2453521.833 | 3 | 7.35, 9.41, 15.60 | 0.55 | 0.45 | 0.24 | 9 | 16.4 |
| 13 | 09/19/05 | 2453632.908 | 2 | 6.0 | 0.72 | N/A | N/A | 31 | 13.2 |
| 14 | 09/20/05 | 2453633.602 | 3 | 6.0, 7.7, 12.8 | 0.99 | 1.00 | 0.52 | 30 | 11.1 |
| 15 | 09/21/05 | 2453634.513 | 3 | 6.0, 7.7, 12.8 | 0.89 | 0.89 | 0.33 | 29 | 11.3 |

Table 1. Engineering runs for the GLAO experiment at Magellan.

to characterize the ground-layer behavior at any given time, and inexpensive hard disk drives provide adequate storage capacity. Exposure start times are controlled through the use of a common trigger voltage sent to all of the cameras. Time synchronization of the frames recorded by separate computers can be a problem because of local clock drift between computers and occasional dropped frames. For this reason a pattern of randomly spaced 1 and 2 millisecond pauses is imposed on the basic 100 Hz trigger signal, which establishes a unique time sync pattern which can be recovered by looking at the difference in time stamps between frames. The hardware setup allowed for continuous recording of data and all the frames were saved to disk for later processing.

3. OBSERVING RUNS

We conducted five observing runs over two years (2004 and 2005), mostly using engineering time and sharing the telescope most nights with other tests or science observations. The first run was used to field test the hardware and work on the software. The other four runs produced 11 nights of wide-field, 100 Hz wavefront sensing data. Typically the setup would take half an hour per camera and then once all the cameras were aligned, the wavefront sensing data would be recorded for approximately ten minutes. Setup involved initializing the hardware and then the aligning the pupil on the lenslet array in each wavefront sensor.

Table 1 lists the parameters of each data set. The number of cameras and sampled baselines between the cameras are listed in columns 4 and 5. The seeing from the Clay guider, DIMM and MASS instruments are listed in columns 6-8. These seeing measurements are the averages in the ten minutes prior to the observation end time (listed as a Julian Date in column 3). All of the seeing measurements have been corrected for airmass and to a reference wavelength of $0.5 \mu m$. The wind speed and temperature are reported as the average conditions for ten minutes surrounding the observation.

4. REDUCTIONS/RESULTS

The imaging data was corrected for bias offsets, binned two by two and smoothed with a double pass 3×3 box car filter, which eliminates sharp peaks and cosmic rays and minimizes centroid errors. Centroids, with sub-pixel accuracy, were obtained by a linear interpolation around the brightest pixel in each sub-aperture. The results from this fast and simple centroiding method differed from a more precise, moment centroiding analysis by less than 0.08 pixels rms. A reference image was built from roughly six thousand frames (60 seconds of data) and used to define the zero-deviation, reference positions for the Shack-Hartmann analysis.

A 36-mode Zernike decomposition (complete up to 6th radial+azimuthal order) was performed on each instantaneous image from the Shack-Hartmann imaging. The end product of the data reduction is a time-series of Zernike coefficients for each camera. Typically 12,000 frames (2 minutes) of data are analyzed. Note that the tip/tilt terms include both atmospheric effects and tracking errors of the mount, particularly wind-shake. During the observations guide corrections were sent to the mount using the standard guide cameras in the usual way, with a response time of about one second.

Since GLAO reduces the wavefront error but typically does not result in diffraction-limited images, it is useful to be able to consider the effect of the Zernike modes as quadrature contributions to the RMS image diameter in arcseconds. Higher-order modes produce larger images for a given wavefront error because the slope errors occur over shorter scales. Table 2 presents a list of conversion factors expressed in arcseconds per micron of wavefront error. The table was derived using Zernike phase screens in a Zemax model of a perfect 6.5 meter telescope. Note that the RMS image diameter is determined from the image centroid, which in the case of coma and higher-order coma may neglect some of the error which shows up as a shift in the image centroid.

Table 3 is a summary of the properties of the Zernike analysis of each run. Column 2 is the seeing as observed through the 59 cm sub-apertures. This number is derived from the total wavefront error (col 3), the fractional wavefront errors observed in each Zernike order (col 4-10) and the conversion factors given in Table 2.

Figure 1 shows an example of the RMS of the Zernike amplitudes for Run 11. The overall shape of the RMS as a function of mode is predicted by atmospheric theory and is useful for deriving measurements of r_o , the outer scale, and testing the validity of Kolmogorov turbulence (to be done in a future study in combination with full presentation of seeing monitor data). Note that there is some variation in the overall RMS from camera

| Zernike Mode | RMS | Zernike Mode | RMS |
|----------------|--|--------------|--|
| | <i>(arcsec/μm)</i> | | <i>(arcsec/μm)</i> |
| 2,3 (Tip/Tilt) | 0.13 | 20, 21 | 1.04 |
| 4 (Focus) | 0.63 | 22 | 2.74 |
| 5,6 (Astig) | 0.45 | 23, 24 | 2.59 |
| 7,8 (Coma) | 0.91 | 25, 26 | 2.13 |
| 9,10 (Trefoil) | 0.64 | 27, 28 | 1.26 |
| 11 (Spherical) | 1.50 | 29, 30 | 3.41 |
| 12, 13 | 1.35 | 31, 32 | 3.18 |
| 14, 15 | 0.84 | 33, 34 | 2.54 |
| 16, 17 | 1.95 | 35, 36 | 1.47 |
| 18, 19 | 1.73 | | |

Table 2. Image Diameter RMS (arcsec) per Micron of Wavefront Error.

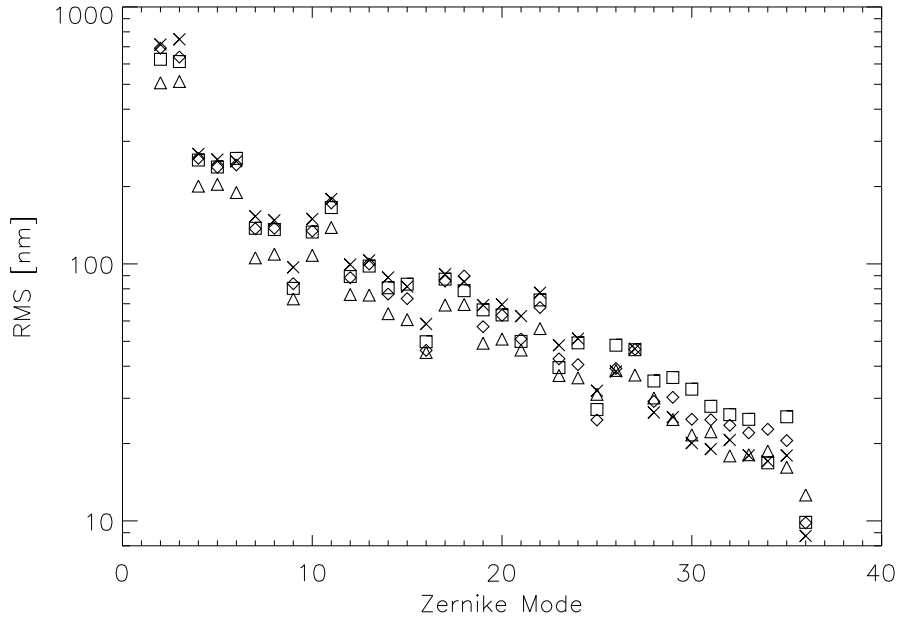


Figure 1. Example of the RMS of the Zernike modes in nm of wavefront error. The four different symbols represent the four cameras from Run 11.

to camera. This is due partly to fainter stars having noisier measurements, but also partly to small variations in the spacing of the optics in the wavefront sensors. The optical effect also includes focus errors caused by the curvature of the telescope focal plane, although we attempt to correct for this during the setup for each observation. To move the measurements on a common scale, the values for each wavefront sensor are scaled to the average for all wavefront sensors in a data set.

The RMS as a function of Zernike mode is plotted in arcseconds in Figure 2. Most of the modes contribute comparably to the total seeing, although it is clear that the contribution is falling off after mode 30 and the radial terms (4, 11, 22) contribute more than the average mode. Also note that although 75% of the wavefront variance is contained in tip/tilt (Table 3), the contribution to RMS image size from these two modes is quite small.

| Run | Seeing | $rms(Z_{total})(nm)$ | $\frac{\langle Z_{tip/tilt}^2 \rangle}{\langle Z_{total}^2 \rangle}$ | $\frac{\langle Z_{order=1}^2 \rangle}{\langle Z_{total}^2 \rangle}$ | $\frac{\langle Z_{order=2}^2 \rangle}{\langle Z_{total}^2 \rangle}$ | $\frac{\langle Z_{order=3}^2 \rangle}{\langle Z_{total}^2 \rangle}$ | $\frac{\langle Z_{order=4}^2 \rangle}{\langle Z_{total}^2 \rangle}$ | $\frac{\langle Z_{order=5}^2 \rangle}{\langle Z_{total}^2 \rangle}$ | $\frac{\langle Z_{order=6}^2 \rangle}{\langle Z_{total}^2 \rangle}$ |
|---------|--------|----------------------|--|---|---|---|---|---|---|
| 1 | 0.37 | 1100 | 0.519 | 0.297 | 0.066 | 0.055 | 0.026 | 0.025 | 0.012 |
| 2 | 0.78 | 1520 | 0.780 | 0.119 | 0.039 | 0.036 | 0.016 | 0.008 | 0.002 |
| 3 | 0.72 | 1520 | 0.810 | 0.107 | 0.032 | 0.029 | 0.013 | 0.006 | 0.002 |
| 4 | 0.62 | 1240 | 0.791 | 0.117 | 0.036 | 0.031 | 0.015 | 0.008 | 0.002 |
| 5 | 0.69 | 1380 | 0.782 | 0.123 | 0.038 | 0.033 | 0.015 | 0.008 | 0.002 |
| 6 | 0.66 | 1070 | 0.706 | 0.146 | 0.055 | 0.053 | 0.022 | 0.013 | 0.004 |
| 7 | 0.87 | 1680 | 0.770 | 0.127 | 0.040 | 0.036 | 0.016 | 0.008 | 0.002 |
| 8 | 1.39 | 2610 | 0.782 | 0.113 | 0.039 | 0.036 | 0.016 | 0.009 | 0.004 |
| 9 | 0.75 | 1380 | 0.752 | 0.135 | 0.044 | 0.040 | 0.018 | 0.009 | 0.003 |
| 10 | 0.86 | 1780 | 0.800 | 0.112 | 0.035 | 0.031 | 0.014 | 0.007 | 0.002 |
| 11 | 0.64 | 1060 | 0.706 | 0.152 | 0.053 | 0.049 | 0.023 | 0.012 | 0.004 |
| 12 | 0.41 | 860 | 0.734 | 0.139 | 0.048 | 0.044 | 0.021 | 0.011 | 0.003 |
| 13 | 0.72 | 1850 | 0.882 | 0.060 | 0.023 | 0.021 | 0.009 | 0.005 | 0.001 |
| 14 | 1.17 | 2330 | 0.799 | 0.105 | 0.038 | 0.034 | 0.014 | 0.008 | 0.001 |
| 15 | 0.61 | 1130 | 0.767 | 0.122 | 0.042 | 0.039 | 0.017 | 0.009 | 0.002 |
| Average | 0.75 | 1500 | 0.756 | 0.134 | 0.043 | 0.038 | 0.017 | 0.009 | 0.003 |

Table 3. Total Wavefront Aberrations and Modal Contribution to Total.

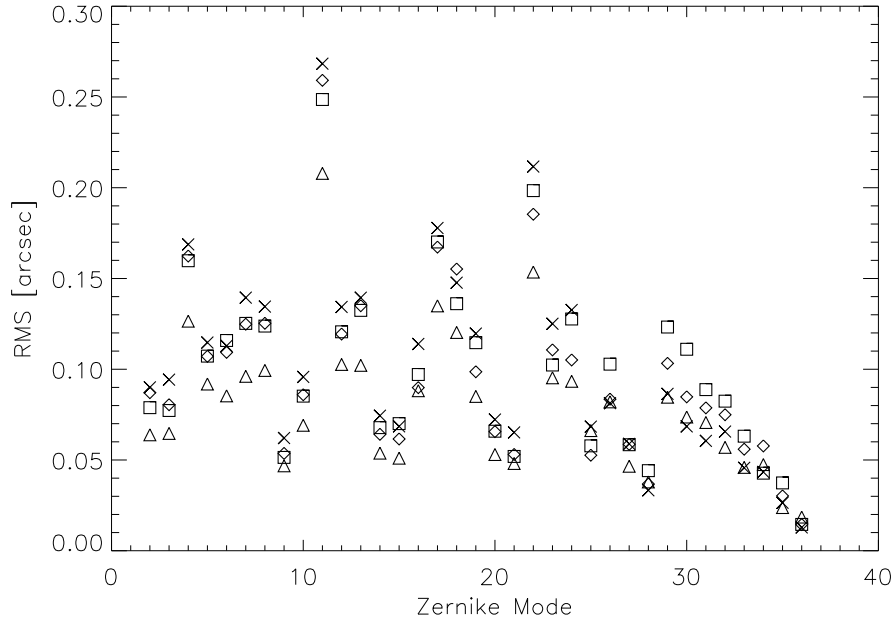


Figure 2. Example of the contribution to the total image diameter of the Zernike modes in arcsec. The four different symbols represent the four cameras from Run 11.

Figure 3 shows the seeing from the Clay guide camera compared with the seeing determined from the wavefront sensors. On average, the 59 cm sub-apertures of our wavefront sensors detect 86% of the variance of the total seeing. This implies that any fractional ground-layer contribution that we measure applies only to the 86% of the seeing that we detect. Presumably the “missing seeing” is in higher order modes, which will have small isoplanatic scale lengths and little impact in a GLAO system.

5. GLAO ANALYSIS

For each pair of cameras, we decompose the wavefront errors in each Zernike mode into a correlated component, Z_G , which we attribute to the ground-layer and an uncorrelated component, Z_U , which we attribute to the upper atmosphere. Any noise associated with the system is also attributed to Z_U , since the upper atmosphere is effectively noise for a system attempting to sense the ground-layer. Then for wavefront sensors 1 and 2, the wavefront errors are $Z_1 = Z_G + Z_{U,1}$ and $Z_2 = Z_G + Z_{U,2}$, where $Z_{U,\#}$ is the upper atmosphere turbulence seen through each wavefront sensor and Z_G is common to both cameras by definition. Define $P \equiv Z_1 + Z_2$, and $M \equiv Z_1 - Z_2$. The variance of P is $\langle P^2 \rangle = 4 \langle Z_G^2 \rangle + 2 \langle Z_U^2 \rangle$ and the variance of M is $\langle M^2 \rangle = 2 \langle Z_U^2 \rangle$. The fraction of the variance arising from the ground-layer is $GL \equiv \frac{\langle Z_G^2 \rangle}{\langle Z_G^2 \rangle + \langle Z_U^2 \rangle} = \frac{\langle P^2 \rangle - \langle M^2 \rangle}{\langle P^2 \rangle + \langle M^2 \rangle} =$

In Table 4 we report the fraction of atmospheric wavefront variance seen in the ground-layer as a function of Zernike radial order. Where multiple baselines were observed within a run, each is reported as a separate line. Tip and tilt are not distinct from mount shake and may not reflect the ground-layer seeing. In the high wind data, Runs 13-15, a clear elongation is seen of the spots, indicating some mount shake. In the next section we put these eleven nights of ground-layer into context and convert these fractional variance measures into image size. As a consistency check, two observations from separate nights were analyzed with this method. These data which are known to be completely uncorrelated produced results of $GL < 0.02$ for all orders. We note that Run 8 is very close to zero and not consistent with the other runs in any of the modes. We are in the process of reexamining this dataset more closely.

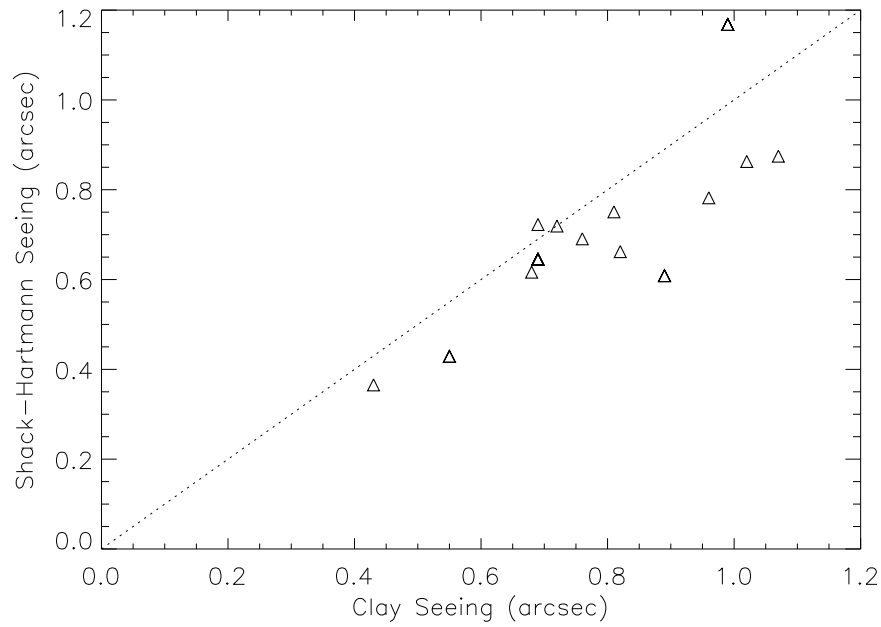


Figure 3. The Clay seeing is plotted against the seeing detected in the 59 cm sub-apertures of the GLAO experiment. The dotted line represents the 1:1 relation. All seeing measurements have been corrected to a reference wavelength of $0.5\mu m$. The 59 cm sub-apertures detect 86% of the total atmospheric variance.

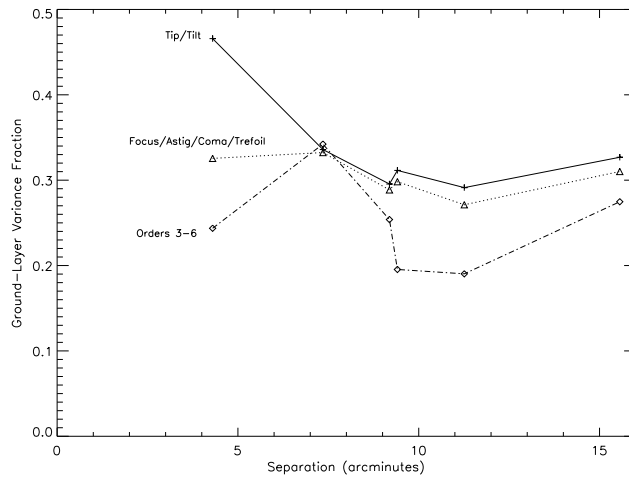


Figure 4. Example of the field effect of the ground-layer. The six baselines are plotted for Run 11. Modes are averaged together to provide increased signal-to-noise.

In Figure 4 the fraction of variance in the ground-layer, GL , is plotted against separation for Run 11. The expected behavior is that the ground-layer contribution will fall off as field angle to the $5/3$ power. However the ground-layer fraction appears to fall off more slowly or even remain approximately constant as field angle increases.

| Run | Separation | $GL_{tip/tilt}$ | $GL_{order=1}$ | $GL_{order=2}$ | $GL_{order=3}$ | $GL_{order=4}$ | $GL_{order=5}$ | $GL_{order=6}$ | All Modes Weighted |
|-----|------------|-----------------|----------------|----------------|----------------|----------------|----------------|----------------|--------------------|
| 1 | 7.04 | 0.33 | 0.24 | 0.13 | 0.14 | 0.13 | 0.10 | 0.07 | 0.112 |
| 2 | 13.85 | 0.49 | 0.22 | 0.23 | 0.20 | 0.17 | 0.15 | 0.13 | 0.208 |
| 3 | 13.85 | 0.60 | 0.20 | 0.09 | 0.04 | 0.05 | 0.06 | 0.06 | 0.100 |
| 4 | 13.85 | 0.60 | 0.36 | 0.29 | 0.23 | 0.20 | 0.17 | 0.14 | 0.257 |
| 5 | 13.85 | 0.46 | 0.25 | 0.16 | 0.15 | 0.13 | 0.12 | 0.11 | 0.172 |
| 6 | 14.88 | 0.27 | 0.23 | 0.27 | 0.35 | 0.33 | 0.29 | 0.29 | 0.308 |
| 7 | 15.54 | 0.31 | 0.15 | 0.13 | 0.10 | 0.09 | 0.09 | 0.10 | 0.116 |
| 8 | 14.88 | 0.02 | 0.03 | 0.04 | 0.05 | 0.03 | 0.04 | 0.02 | 0.039 |
| 9 | 15.54 | 0.21 | 0.19 | 0.19 | 0.17 | 0.19 | 0.16 | 0.15 | 0.182 |
| 10 | 12.90 | 0.18 | 0.08 | 0.06 | 0.07 | 0.03 | 0.05 | 0.04 | 0.068 |
| 11 | 4.30 | 0.46 | 0.36 | 0.29 | 0.29 | 0.26 | 0.18 | 0.13 | 0.272 |
| | 7.35 | 0.34 | 0.34 | 0.32 | 0.38 | 0.35 | 0.30 | 0.21 | 0.336 |
| | 9.19 | 0.31 | 0.30 | 0.30 | 0.25 | 0.19 | 0.15 | 0.09 | 0.227 |
| | 9.41 | 0.30 | 0.30 | 0.28 | 0.30 | 0.26 | 0.20 | 0.13 | 0.279 |
| | 11.26 | 0.29 | 0.31 | 0.24 | 0.25 | 0.19 | 0.13 | 0.08 | 0.219 |
| | 15.56 | 0.32 | 0.31 | 0.31 | 0.33 | 0.28 | 0.22 | 0.14 | 0.291 |
| 12 | 7.35 | 0.44 | 0.42 | 0.34 | 0.34 | 0.34 | 0.28 | 0.24 | 0.336 |
| | 9.41 | 0.46 | 0.33 | 0.24 | 0.21 | 0.19 | 0.13 | 0.10 | 0.217 |
| | 15.86 | 0.35 | 0.28 | 0.23 | 0.25 | 0.22 | 0.16 | 0.12 | 0.226 |
| 13 | 6.0 | 0.75 | 0.36 | 0.16 | 0.17 | 0.10 | 0.07 | 0.02 | 0.198 |
| 14 | 6.00 | 0.72 | 0.66 | 0.44 | 0.39 | 0.38 | 0.26 | 0.20 | 0.449 |
| | 7.70 | 0.62 | 0.45 | 0.24 | 0.19 | 0.12 | 0.07 | 0.06 | 0.231 |
| | 12.90 | 0.74 | 0.39 | 0.17 | 0.09 | 0.01 | 0.02 | <0.01 | 0.157 |
| 15 | 6.00 | 0.79 | 0.70 | 0.60 | 0.54 | 0.49 | 0.35 | 0.24 | 0.535 |
| | 7.70 | 0.83 | 0.72 | 0.57 | 0.54 | 0.44 | 0.32 | 0.18 | 0.519 |
| | 12.90 | 0.69 | 0.64 | 0.54 | 0.50 | 0.46 | 0.33 | 0.21 | 0.497 |

Table 4. Fraction of Variance Detected in Ground-Layer

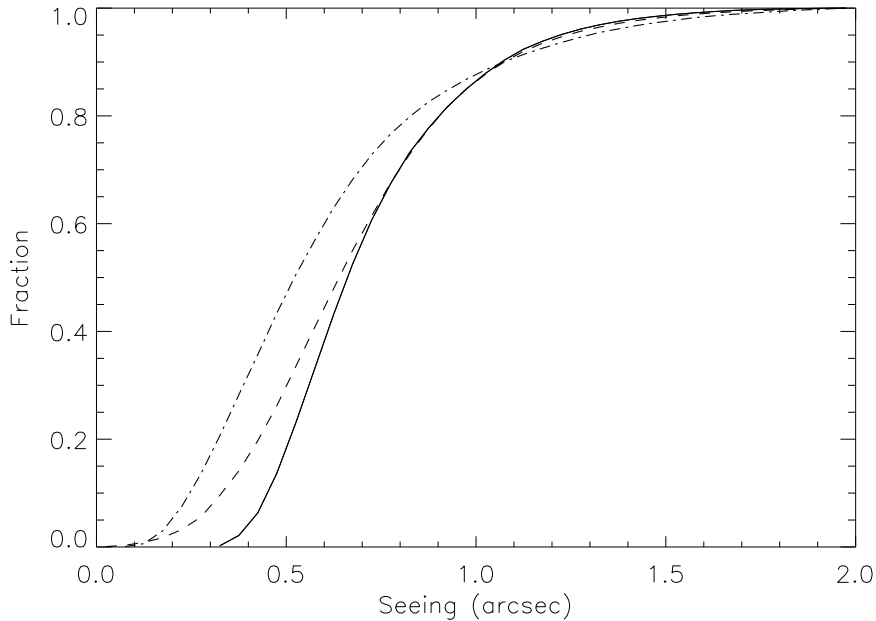


Figure 5. Cumulative seeing histogram for Clay (solid), DIMM (dash), MASS (dot-dash) for one-year's worth of data. See Table 6 for quartile seeing values.

6. SUPPORTING DATA

In order to put the GLAO experiment data into context, we have examined a year's worth of site monitoring data. Meteorological data are being collected at the Magellan site using weather stations manufactured by Davis Instruments Corp. A Weather Monitor II station has been in continuous operation at site since late-2000. In 2005 this station was replaced with two newer models (Vantage Pro & Vantage Pro2) which utilize the same basic sensor technology to measure temperature, humidity, atmospheric pressure, and wind speed and direction. The stations generate measurements for temperature, pressure, humidity, wind speed, and wind direction every 1-2 seconds and are stored in a database as 1 minute averages.

The seeing is being monitored at the Magellan telescopes through the use of a differential image motion monitor (DIMM). The DIMM¹¹ functions by using Kolmogorov turbulence theory to relate the FWHM of a long exposure in a large telescope to the variance in the difference in the positions of two images of the same star created by placing two weak prisms at the aperture of a small telescope. The Magellan DIMM is based on the CTIO RoboDIMM, but has several improvements. Following a technique developed by the TMT project, software was written to use a SBIG ST7 CCD in a drift scan readout mode which allows for many more image motion measurements to be made per minute and thus improved statistics. Image quality has also been improved by using two thinner prisms as opposed to one thicker prism and an open aperture.

Turbulence in the atmosphere above 500 m is being monitored by a multi-aperture scintillation sensor (MASS,¹²). The spatial scale of the scintillation variation depends on the distance to the turbulence which gives rise to the wavefront phase disturbance. The turbulence distribution in a small number of discrete layers can be determined by fitting a model to the differences between the scintillation indices within four concentric apertures. Our MASS has an accompanying DIMM built into it. This instrument, known as a MASS-DIMM, was fabricated and provided by CTIO and put into operation in a tower at the Magellan telescopes site. The MASS-DIMM instrument operates at the back-end of a 0.25 meter Meade telescope in its own, ventilated 10-meter tower. The MASS is only sensitive to turbulence above 500 m. In addition to the turbulence profile, the MASS also measures free atmospheric seeing (essentially the integral of the turbulence profile), the adaptive

| Percentile | MASS | DIMM | Clay |
|------------|------|------|------|
| 10% | 0.25 | 0.33 | 0.45 |
| 25% | 0.35 | 0.47 | 0.53 |
| 50% | 0.52 | 0.64 | 0.66 |
| 25% | 0.75 | 0.85 | 0.84 |
| 10% | 1.07 | 1.07 | 1.07 |

Table 5. Seeing Percentiles for MASS, DIMM, and Clay

optics time constant and the isoplanatic angle. The difference between the DIMM seeing and the free atmosphere MASS seeing is a measure of the seeing contributed by the ground layer.

In addition to the site monitoring equipment, the seeing from both Magellan Telescopes is recorded automatically. The Magellan guide cameras have low quality optics with significant aberrations and so a correction (0.35" in quadrature) must be removed from the observed FWHM values. The guide cameras use a RG610 filter and that combined with the midband coated E2V CCD47-20 produces an effective wavelength of 765 nm.

We examined 205 nights from March 2004 to April 2005 that had both seeing measurements from all the instruments and meteorological data. (Note that the clear fraction of nights is higher, but the MASS-DIMM instrument was being commissioned in the first half of 2004.) For each seeing measurement, a mean temperature, pressure, wind speed and wind direction was defined as the mean meteorological condition for 15 minutes surrounding the seeing measurement. In the end, we assembled 64,000 MASS and 64,000 DIMM seeing measurements and 128,000 Clay guide camera seeing measurements. All of the data were corrected to an airmass of 1, and to a reference wavelength of 0.5 μ m. The MASS data were reprocessed with the most recent version of the turbina software.

The first consistency check is to compare the Magellan seeing measurements to the DIMM seeing. In Figure 5 the cumulative seeing histograms are plotted for the Clay guide camera (solid), DIMM (dash), and MASS (dot-dash) and in Table 6 select values are presented numerically. The agreement between the DIMM and Clay is good, but not perfect. The low end difference between the two is likely caused by the simple correction applied to compensate for the guide camera optics. This correction is a first order correction and could likely be improved with further analysis. The effects of an outer scale will suppress the seeing in the larger Clay Telescope aperture. However, since the DIMM is a differential measure (and a much smaller structure), the DIMM seeing values will be unaffected by mount and wind shake. It appears that to first order, these two effects cancel each other out and we obtain good agreement between the Magellan guiders and the DIMM.

The MASS data relative to the DIMM data indicates that in the median conditions, ground-layer is responsible for about 38% of the atmospheric variance. This is a smaller percentage of total seeing than is observed at other sites.^{4,13-15} At Las Campanas, a ground-layer correction would work in the sense of making a good night better as there is little difference seen between the MASS and DIMM at higher seeing values.

In Figure 6 the ground-layer as measured by MASS-DIMM, $(1 - \frac{MASS^2}{DIMM^2})$, is plotted against the trends lines for ground-layer fractional variance as measured by our experiment. We set any MASS-DIMM data that results in a negative value to zero and attribute this to noise and small errors in the absolute calibration between the two instruments. There is a correlation in between the MASS-DIMM and the GLAO experiment, although the relationship is far from one-to-one. The crosses are the data that were used to determine the trend-line for orders 3-6 and provide a sense of the uncertainties. It is interesting to note that even when the MASS-DIMM indicates that there is no ground-layer, there is a significant tip/tilt correlation, indicating that approximately 30% of the variance in tip/tilt is due to mount shake.

There is also a small offset in the higher order modes. Since a GL measurement between two separate nights produced a result of less than 0.02, the positive values of about 0.1 in the higher-order modes, even when the MASS-DIMM comparison fails to detect the ground layer, are likely to be significant.

Figure 7 shows the ground-layer as measured by MASS-DIMM and the RMS image improvement. These numbers were derived by reducing each mode in the RSS of the total variance by the amount of observed

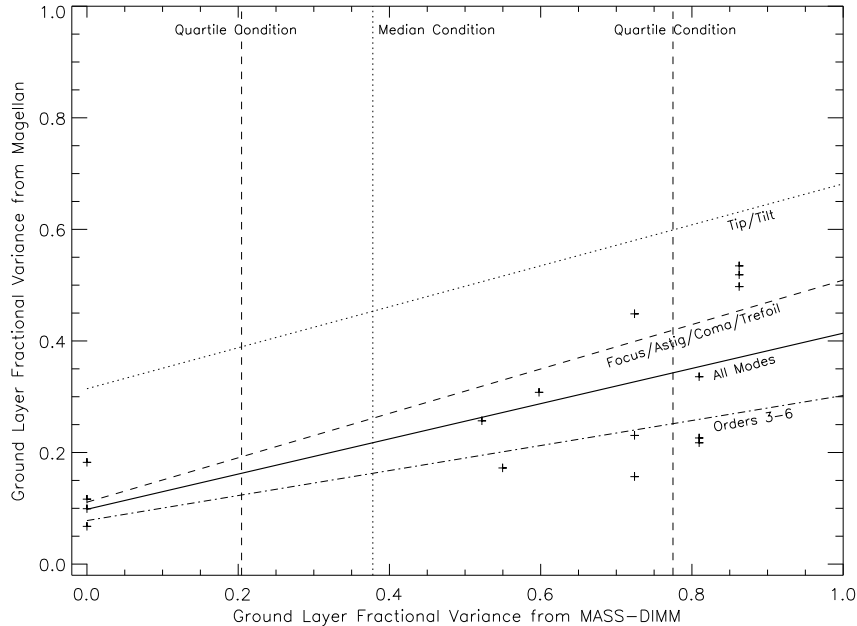


Figure 6. MASS-DIMM measured ground-layer vs ground-layer from this experiment. The mean relation between ground-layer variance as measured by the MASS-DIMM instrument and the Magellan Telescope is plotted as a solid line and labeled All Modes. The data for All Modes are plotted as crosses to provide a sense of the errors. Trend-lines for tip/tilt (dot), Focus, Astigmatism, Coma, Trifoil (dashed), and higher orders (dot-dash) are drawn as a fit to the data from Table 5. The vertical lines indicate the quartile conditions as determined from a year’s worth of seeing data.

ground-layer reduction (Table 4). These scaled variances are then converted to arcseconds and compared to the uncorrected RSS variance from the same data. These calculations include the scaling factor that accounts for the fact that the 59 cm sub-apertures only see 86% of the seeing.

The largest gains are obtained when the MASS-DIMM reports the strongest ground-layer. Note that multiple points will show up for a given observation if more than one baseline was observed. It is clear that strong ground-layer nights allow for improvements in image quality, although the amount of improvement is significantly less than predicted. Neither of the two previous figures are changed significantly by the removal of the largest (>10 arcmin) baseline data. The strongest ground-layer night also happened to be the night of the strongest winds (and technically over the operating limit!). However, no correlation exists between image correction and ground wind speed.

7. CONCLUSION

We have taken one of the first sets of moderate speed (100 Hz), wide-field (arcminutes), and moderate resolution (59 cm sub-aperture) wavefront sensor data, in order to assess the gains of a GLAO system. We have taken this data on eleven nights which span a range of meteorological, seeing, and reported ground-layer strength conditions. On the best nights, we find a RMS image size reduction of 30% over a 7 arcminute separation. On a typical night we find a 10% correction to a visible-band image.

ACKNOWLEDGMENTS

This work has been supported by the Seaver Foundation. We are very grateful to I. Thompson for sharing telescope time with this project. We would also like to thank the staff of Las Campanas.

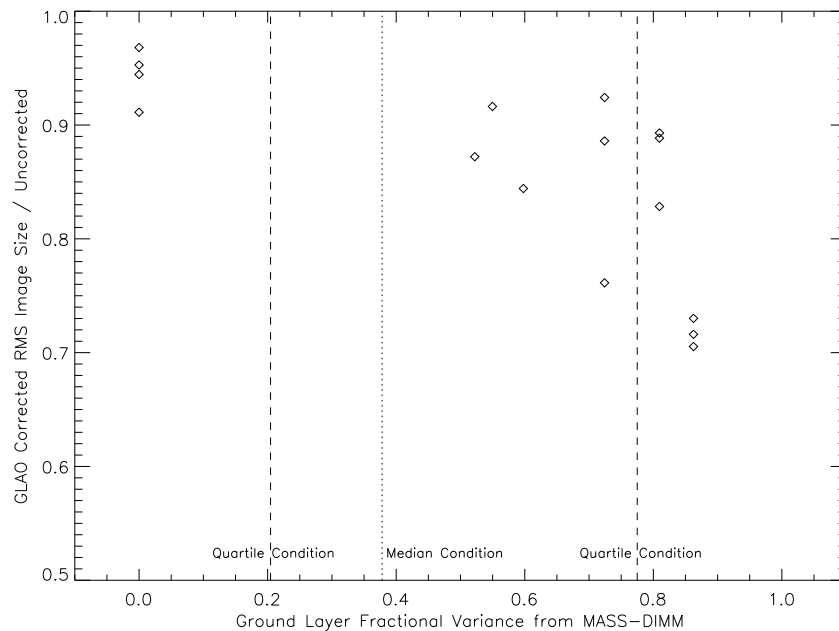


Figure 7. Improvement in RMS images diameter shown as a function of MASS-DIMM reported ground-layer. Vertical lines indicate the quartile and median conditions. Note that not all the runs have MASS-DIMM data, and each baseline for a given run is plotted, providing multiple measurements for some nights. This calculation includes a correction to account for the fact that 86% of the total seeing variance is observed in the 59 cm sub-apertures.

REFERENCES

1. J. Vernin and C. Munoz-Tunon, “Optical seeing at La Palma Observatory. 2: Intensive site testing campaign at the Nordic Optical Telescope,” *A&A* **284**, pp. 311–318, Apr. 1994.
2. V. A. Klueckers, N. J. Wooder, T. W. Nicholls, M. J. Adcock, I. Munro, and J. C. Dainty, “Profiling of atmospheric turbulence strength and velocity using a generalised SCIDAR technique,” *A&AS* **130**, pp. 141–155, May 1998.
3. R. Avila, J. Vernin, and L. J. Sánchez, “Atmospheric turbulence and wind profiles monitoring with generalized scidar,” *A&A* **369**, pp. 364–372, Apr. 2001.
4. A. Tokovinin, S. Baumont, and J. Vasquez, “Statistics of turbulence profile at Cerro Tololo,” *MNRAS* **340**, pp. 52–58, Mar. 2003.
5. L. J. Sánchez, D. X. Cruz, R. Avila, A. Agabi, M. Azouit, S. Cuevas, F. Garfias, S. I. González, O. Harris, E. Masciadri, V. G. Orlov, J. Vernin, and V. V. Voitsekhovich, “Contribution of the surface layer to the seeing at San Pedro Mártir: Si-mul-ta-neous microthermal and DIMM measurements,” in *Revista Mexicana de Astronomía y Astrofísica Conference Series*, pp. 23–30, Sept. 2003.
6. R. W. Wilson and C. Saunter, “Turbulence profiler and seeing monitor for laser guide star adaptive optics,” in *Adaptive Optical System Technologies II. Edited by Wizinowich, Peter L.; Bonaccini, Domenico. Proceedings of the SPIE, Volume 4839, pp. 466-472 (2003).*, pp. 466–472, Feb. 2003.
7. F. J. Rigaut, B. L. Ellerbroek, and R. Flicker, “Principles, limitations, and performance of multiconjugate adaptive optics,” in *Proc. SPIE Vol. 4007, p. 1022-1031, Adaptive Optical Systems Technology, Peter L. Wizinowich; Ed.*, pp. 1022–1031, July 2000.
8. A. A. Tokovinin, B. Gregory, H. E. Schwarz, V. Terebizh, and S. Thomas, “A visible-light AO system for the 4.2m SOAR telescope,” in *Adaptive Optical System Technologies II. Edited by Wizinowich, Peter L.; Bonaccini, Domenico. Proceedings of the SPIE, Volume 4839, pp. 673-680 (2003).*, P. L. Wizinowich and D. Bonaccini, eds., pp. 673–680, Feb. 2003.

9. R. W. Wilson, J. Bate, J. C. Guerra, N. N. Hubin, M. Sarazin, and C. D. Saunter, "Development of a portable SLODAR turbulence profiler," in *Advancements in Adaptive Optics. Edited by Domenico B. Calia, Brent L. Ellerbroek, and Roberto Ragazzoni. Proceedings of the SPIE, Volume 5490, pp. 758-765 (2004).*, D. Bonaccini Calia, B. L. Ellerbroek, and R. Ragazzoni, eds., pp. 758–765, Oct. 2004.
10. M. Lloyd-Hart, C. Baranec, N. M. Milton, T. Stalcup, M. Snyder, N. Putnam, and J. R. P. Angel, "First Tests of Wavefront Sensing with a Constellation of Laser Guide Beacons," *ApJ* **634**, pp. 679–686, Nov. 2005.
11. M. Sarazin and F. Roddier, "The ESO differential image motion monitor," *A&A* **227**, pp. 294–300, Jan. 1990.
12. A. A. Tokovinin, "A new method of measuring atmospheric seeing," *Astronomy Letters* **24**, pp. 662–664, Sept. 1998.
13. A. Tokovinin and T. Travouillon, "Model of optical turbulence profile at Cerro Pachón," *MNRAS* **365**, pp. 1235–1242, Feb. 2006.
14. A. E. Gur'yanov, M. A. Kallistratova, A. S. Kuttyrev, I. V. Petenko, P. V. Shcheglov, and A. A. Tokovinin, "The contribution of the lower atmospheric layers to the seeing at some mountain observatories," *A&A* **262**, pp. 373–381, Aug. 1992.
15. R. W. Wilson, "SLODAR: measuring optical turbulence altitude with a Shack-Hartmann wavefront sensor," *MNRAS* **337**, pp. 103–108, Nov. 2002.